Impact of Morphology, Side-Chains, and Crystallinity on Charge-Transport Properties of π-Extended Double Helicenes

Impact of Morphology, Side-Chains, and Crystallinity on Charge-Transport Properties of π-Extended Double Helicenes

Ilhan Yavuz,[†] Janice B. Lin,[‡] and K. N. Houk[‡§]*

[†] Department of Physics, Marmara University, 34722, Ziverbey, Istanbul, Turkey

[‡] Department of Chemistry and Biochemistry, University of California, Los Angeles, California 90095

[§]Department of Chemical and Biomolecular Engineering, University of California, Los Angeles, California 90095

AUTHOR INFORMATION

Corresponding Authors

*ilhan.yavuz@marmara.edu.tr

ABSTRACT. We report a computational study on the effect of side-chain substitution, heteroaromatic substitution and unique crystal packing on the charge transport and mobility of three double helicene molecules. These double helicene (DH1) molecules, having curved π-conjugation, are structural hybrids of non-planar [6]helicene and planar tribenzo[b,n,pqr]perylene (TBP). We find that side-chain substitution has small effect on intrinsic electronic properties in DHs but dramatically impacts the packing arrangement, morphologies and transport network, exhibited in calculated charge transport parameters. Interestingly, the dimensionality of the transport evolves from one dimensional to three dimensional with side-chain substitution (DH2) and then heteroaromatic substitution (DH3). Using two different pwell-known transport models, we have established a direct link between the morphology, transport connectivity, and hole mobilities. While both unsubstituted and substituted DHs have high hole mobilities in the ordered phase, the results show that with inclusion of positional disorder, the mobilities of disordered DH1 and DH3 lowered while the mobility of DH2 remained nearly unchanged. We relate this effect to the dimensionality of their unique transport networks. These DH molecules are promising organic semiconductors with high mobilities in ordered and disordered phases, with predicted values that lie in the range of ~1 to 10 cm^2 V^{-1} s^{-1}.

I. Introduction

Polycyclic aromatic hydrocarbons (PAHs) have been of interest in the scientific community as organic semiconductors in field-effect transistors (FETs), light-emitting diodes (LEDs), and organic photovoltaics (OPVs). Most PAHs are two-dimensional, achiral materials that typically pack in a herringbone or lamellar manner. While these materials exhibit high mobilities and interesting optoelectronic properties, molecular ordering must be precisely controlled through functionalization of PAHs.[1,2,3] In the last 100 years, interest has evolved towards curved aromatic hydrocarbons, such as corannulenes and helicenes, that are three-dimensional and can be either chiral or achiral. Nuckolls advanced the idea of "contorted aromatics" as electronic materials years ago[4] and has since applied these materials as acceptor materials in OPVs[5,6,7] photodetectors,[8] and columnar-structured OFETs.[9] These materials usually pack in a columnar manner or with partial π-π stacking, which allows for close orbital contacts between molecules for high multi-dimensional charge transport.[10,11,12]

In particular, helical structures have been synthesized and studied for a variety of applications, including molecular recognition, asymmetric catalysis, and as conductive

materials.[13] The unusual molecular packing of these molecules can result in varying

properties in the solid state, such as charge transport[14,15,16] and luminscence,[17,18]

important parameters for the implementation of these materials in optoelectronic devices.

Twisted two-dimensional aromatic compounds have found crucial applications as one-

dimensional photoconductors,[19] in small-molecule solar cells,[20] and as stackable

molecules in thin-film transistors.[21] Spiro-fused materials are also important hole

transport materials; for example, spiro-OMeTAD[22,23,24] is considered the state-of-the-art

hole transport material and is used in both dye-sensitized[25,26] and perovskite solar

cells.[27,28,29]

In 2015, Itami and coworkers reported the synthesis and characterization of π-extended

double helicene **DH1** (Scheme 1), which combines the properties of planar [6]helicene

and non-planar tribenzo[*b*,*n*,*pqr*]perylene (TBP).[30] Due to the chiral nature of the

molecule, it packs in a contorted lamellar manner with π-π stacking and close π-π contacts

in two directions. The Itami group published the synthesis and properties of alkylated **DH2**

and dithia[6]helicene **DH3**.[31] Using DFT to calculate the FMOs of the DHs, the group

found that the FMOs have a larger distribution on the TBP π-planes of **DH3** than the other

variants. They also obtained a hole mobility of 3.3×10^{-2} cm^2 V^{-1} s^{-1} with an on/off ratio of greater than 10^5 for **DH3** from a top-contact/bottom-gate FET. The relatively high hole mobility of **DH3**, coupled with the interesting packing properties of these helical molecules, indicate that these molecules are promising candidates as donor materials in organic electronic applications.[32] As a further probe into the factors to dictate the charge transport in these systems, we report a computational study on the effect of side-chain substitution and unique crystal packing on the charge transport of double helical molecules **DH1**, **DH2**, and **DH3**. Using a previously described method rooted in rate-based theory and kinetic Monte Carlo (kMC) simulations,[33] we calculate charge-transport properties and hole mobilities for ordered and disordered DH systems.

The paper is organized as follows: the computational procedure used to predict the atomistic morphology, charge transport parameters and mobility are presented in Section II. In Section III, the results of our atomistic morphology and charge-transport simulations are reported; atomistic morphologies are quantified by root-mean-squared deviations, fluctuations in interblade torsions and paracrystallinity, whereas charge transport are quantified by hole transport reorganization energy, electronic coupling, site-energy,

energetic disorder and hole mobility. Finally, we concluded the paper by a brief summary

in Section IV.

Scheme 1. Double helical molecules of interest in this study

R=H   DH1
R=nBu DH2

DH3
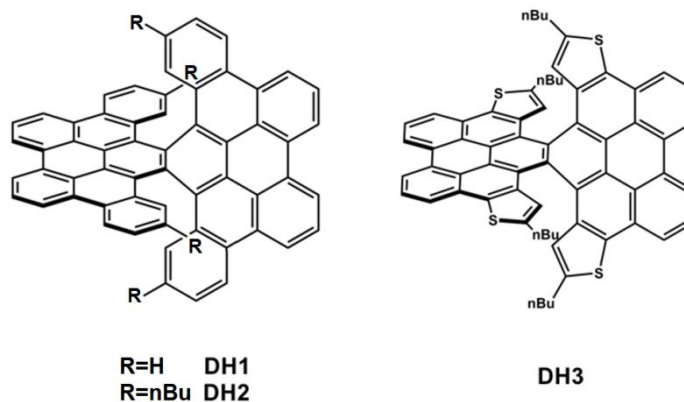
II. Computational Methods

II. 1. Morphology prediction.

A comprehensive method was developed in the Houk group[33] to calculate charge

transport properties of organic crystals and thin-films based on an established charge-

hopping model and MD simulations[34]. While thin-films typically possess large structural

disorder, *e.g.*, due to their polycrystalline morphologies, organic crystals are devoid of

these. Therefore, in this methodology, charge-mobilities of organic materials in the

presence of perfect structural order and structural disorder are benchmarked with experimental organic crystal and thin-film mobilities, respectively. Ordered morphologies are generated from the experimental unit-cells of organic materials, whereas disordered morphologies are generated by incorporating thermal fluctuations to supercells. The workflow has been validated with test sets of over the hole mobilities of 20 electron donor and the electron mobilities of 20 electron acceptor molecules used in OFETs and OPVs for both single crystal and thin film morphologies, for which calculated hole and electron mobilities were predicted well within an order of magnitude.[33,35] We apply this methodology here to calculate single-crystal and thin-film hole transport for **DH1**, **DH2**, and **DH3** .

Experimental crystal structure data for each DH molecule was obtained from refs 12 and 31, which were used as starting structures for the calculations. Initial supercells containing 896, 1024 and 800 molecules (for **DH1**, **DH2**, and **DH3**, respectively) were constructed with periodic boundary conditions (PBC). We considered two morphological phases: (1) ordered phase, with perfect positional order and (2) disordered phase, with incorporation of positional disorder into XRD data. Single-crystal hole mobilities were

computed based on perfect order morphology, and thin-film hole mobilities were modeled

with the introduction of thermal and energetic disorder using atomistic MD simulations to

predict mesoscale ordering, as described earlier.[33]

MD simulations in an NPT ensemble were performed on these systems at 300K using

the GPU version of Amber12.[36,37] GAFF force fields were used for molecular mechanics

parameters, which performs reasonably good for organic solids.[38,39,40] Partial charges of

ground-states were generated from B3LYP/6-311G(d,p)-optimized geometries via the

Merz-Singh-Kollman scheme[41,42] using HF/6-31G(d), as implemented in Gaussian09.[43]

Each supercell was first heated from 0K to 300 K for 2 ns and then NPT equilibrated for

another 2 ns at 300 K while restraining heavy atom positions.[44] A final 20 ns production

run was performed at 300 K and time-averaged pressure at 1 atm. Snapshots of the MD

simulations were taken at various time points in order to obtain atomistic morphologies

for subsequent charge transport calculations. Representative MD snapshots for **DH1**,

DH2, and **DH3** from equilibration at 300K can be found in the Supporting Information.

II. 2. Charge transport.

With the ordered and MD-equilibrated disordered morphologies in hand, we perform charge-carrier dynamics simulations to calculate charge transfer rates using Marcus theory based on incoherent hopping events. Marcus theory relies on two assumptions: (1) charges are instantaneously localized on each site (or molecule, in the case of organic semiconductors)[45,46] and (2) a non-adiabatic charge transfer reaction between molecular pairs occurs through a hopping-type mechanism. Pairs are defined as molecules with centroid distances below 0.8 nm, each of which are added to a neighbor list, a compilation of all possible adjacent hopping sites. Electronic coupling elements, J_{ij}, of the charge-transfer were calculated for defined molecular pairs using DFT(B3LYP/6-31G(d))-based Dimer Projection (DIPRO) method for the ordered phase, and the ZINDO-based Molecular Orbital Overlap (MOO) method for the disordered phase.[47,48,49] However, we also report electronic coupling calculations with ZINDO for ordered phase to make a consistent comparison with the disordered case. Even though the B3LYP method has been shown to perform reasonably good[50], the calculation of J with any DFT method in the disordered phase is computationally prohibitive, because of the number of unique molecular pairs exceeding 20,000 in our study. Therefore, we solely use ZINDO in the

10

disordered case, since its ~50,000 times faster electronic coupling calculation compared

to DFT. More importantly, the electronic couplings and mobilities calculated by the ZINDO

method is fairly reliable, since it sufficiently agrees with those calculated by B3LYP/6-

31G(d) (*vide infra*). Additionally, we perform electronic energy calculations on certain

cohesive molecular pairs in the crystal, based on the B97D/6-311G(d,p) methodology, to

determine the strength of the intermolecular interactions. This DFT methodology is known

to have reasonable predictive power for interaction energies, E_{int}.[51]

The reorganization energy (associated with the local electron-phonon coupling) λ of

each molecule was calculated from the potential energy curves of the ground and charged

state using the four-point rule with B3LYP/6-311G(d,p).

$$\lambda = \left(E_{q_+}^n - E_{q_0}^n \right) + \left(E_{q_+}^c - E_{q_0}^c \right) \tag{1}$$

where, $E_{q_0}^n$ ($E_{q_+}^c$) is the total energy in the gas-phase optimized neutral (charged) state

and $E_{q_0}^c$ ($E_{q_+}^n$) is the total energy of the charged (neutral) state in the optimized neutral

(charged) state. Site energies were calculated self-consistently using Thole Model, which

includes contributions from electrostatic interactions due to polarization and from an

external electric field (see ref. 34 for details). In accordance with the method previously described for MD simulations, partial charges of neutral and charged states were generated via Merz-Singh-Kollman scheme,[40,42] using HF/6-31G(d) method based on B3LYP/6-311G(d,p)-optimized geometries. Isotropic atomic polarizabilities of the neutral and charged states were re-parameterized for each species to calibrate against molecular polarizabilities obtained using B3LYP/6-311G(d,p). Energetic disorders were extracted using the Gaussian Disorder Model (GDM), where the histogram of site energy differences (ΔE_{ij}) were fitted to the following Gaussian distribution and used to extract energetic disorder (σ). Kinetic Monte Carlo (kMC) methods were used to predict charge transport of a charge carrier in an applied external electric field, as implemented in VOTCA, and hole mobilities were obtained using velocity-averaging.[47,52,53]

The possibility for strong coupling between molecular sites opens up an argument on the reliability of this picture of localized charge transport in organic semiconductor systems with a certain degree of order; however, there is ample evidence that rate-based models at room temperature can be employed, with the expense of some error.[54,55,56,33,57,58,59,60,61] To account for a complete picture to include charge carrier

delocalization in the ordered phase, we also calculated charge mobilities using an

analytical approach recently devised by Fratini *et al.*[62] based on localization mapping

(*vide infra*). In this transient localization model, the analytical form of the mobility is given

by the formula $\mu = (e/k_B T)(L^2/2\tau)$, where L is the localization length (in units of lattice

spacing) and τ is the intermolecular structural fluctuation time. The dynamical oscillation

period of these fluctuations ($2\pi\tau$) does not change much for different compounds and can

be taken as 1 ps. The authors built a map of the transient localization lengths in disordered

systems to efficiently determine the mobility of organic semiconductors. We adopt the

arguments given in ref. 60 as an alternative method to calculate mobilities of DHs (see SI

for details).

III. Results & Discussion

III. 1. Molecular Structure, Packing, and Morphology

The packing and solid-state order of **DH1**, **DH2** and **DH3** are calculated using molecular

dynamics simulations and DFT in order to gain a better understanding of their

morphologies. The packing of these structures has been discussed by the Itami group

and full analyses can be found in refs 30 and 31. Here, we discuss the packing of **DH1**,

DH2, and **DH3** in the solid state to establish quantifiable parameters of disorder, which

will be referred to throughout the text. We then use three parameters to quantify the

degree of structural change between the structures: (1) root-mean-square deviation

(RMSD) of the structures, (2) dihedral angle between the TBP blades, and (3)
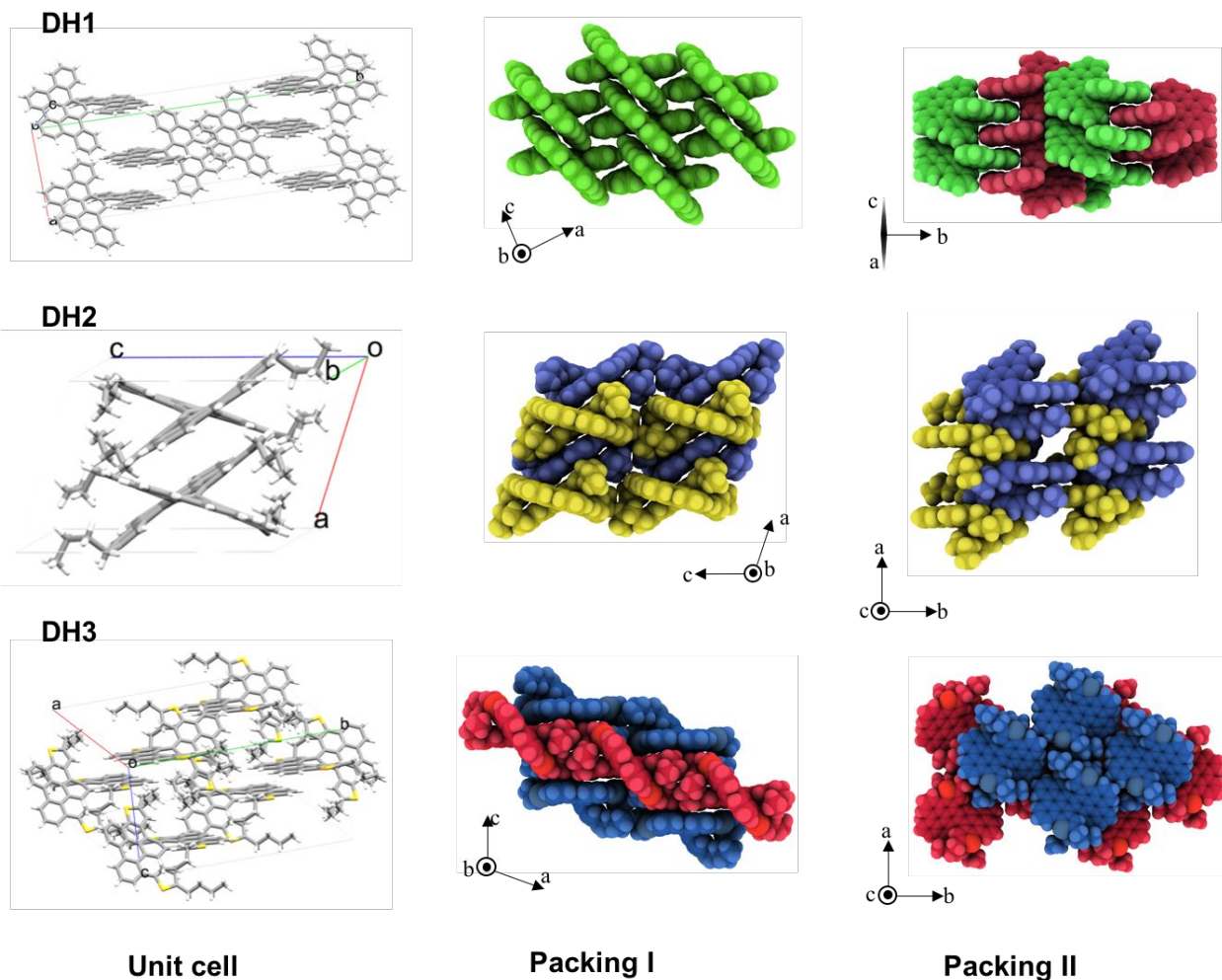
paracrystallinity.

Figure 1. Unit-cells and packing motifs from two angles. Heterochiral packing is indicated by the use of two different colors.

We observed that the impact of the side-chains in the crystallization and the packing motifs of the DH is dramatic. **DH1**, **DH2**, and **DH3** each exhibit 2D packing behavior, where π-blades form intrinsic slipped π-stacking (see Figure 1). For **DH1**, there are two types of interactions by the blades: a slipped π-π stacking interaction (Packing I) and an

edge-to-edge interaction at the interface of the stereoisomers (Packing II). For blades

nearly perpendicular to the a-axis (parallel to the $(30\bar{1})$ plane), the TBP blades pack in a

slipped, but relatively strong (E_{int} = -26 kcal/mol), π-π stacking manner. The blades that

are nearly perpendicular to the c-axis (parallel to the $(\bar{1}02)$ plane) pack relatively weakly

(E_{int} = -10 kcal/mol), as only the edges of the TBPs are in contact. Packing is homochiral

in the [100] and [001] directions (Packing I) and heterochiral in the [010] direction, in

which different isomers are labeled with different colors (Packing II). The interaction

energy in the latter direction is relatively weak with an interaction energy of E_{int} = -18

kcal/mol. For the **DH2** system, there is relatively strong slipped π-π stacking of the TBPs

along the [100] direction, and packing is heterochiral in both [100] and [010] directions.

Specifically, we observe that the distance between the TBP blades is alternating along

[100], as 3.26Å and 3.31 Å. This amounts to an interaction energy of E_{int} = -34 kcal/mol

E_{int} = -29 kcal/mol, respectively. A similar packing arrangement is found in **DH3**, where

there is strong (E_{int} = 32 kcal/mol) and heterochiral π-π stacking of the π-blades along

[001]. Finally, for alkylated derivatives **DH2** and **DH3**, the n-butyl side-chains interfere

with lateral packing ([001] for DH2 and [100] for **DH3**).

To classify the molecular structures of DHs in the solid-state and in the gas phase, we compare the planarity of the π-blades in the solid state with the gas phase DFT-optimized structures. XRD measurements reveal that the blades are planar in the crystal structures of all **DH**s, although DFT-optimized geometries indicate that the blades are slightly helical in the gas phase (Figure 2). The increased planarity in all three systems in the solid state is attributed to stabilizing non-bonding packing forces. These types of interactions are widely observed for conjugated materials such as biphenyl and bithiophene, which are non-planar in the gas phase[63,64] but exhibit low torsional disorder in the solid state when incorporated into oligomers and polymers.[65,66,67,68] For the **DH**s, this change is beneficial in terms of charge-transport, as planarity increases the molecular overlap between molecules and enhances electronic-coupling between molecular pairs.
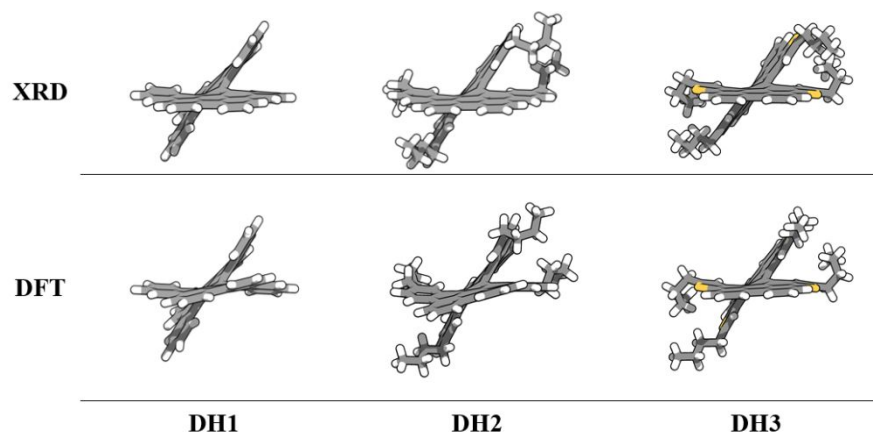
Figure 2. Structures of **DH1**, **DH2**, and **DH3** from (top) X-ray measurements of solid-state structures and (bottom) gas-phase B3LYP/6-311G(d,p) optimizations.
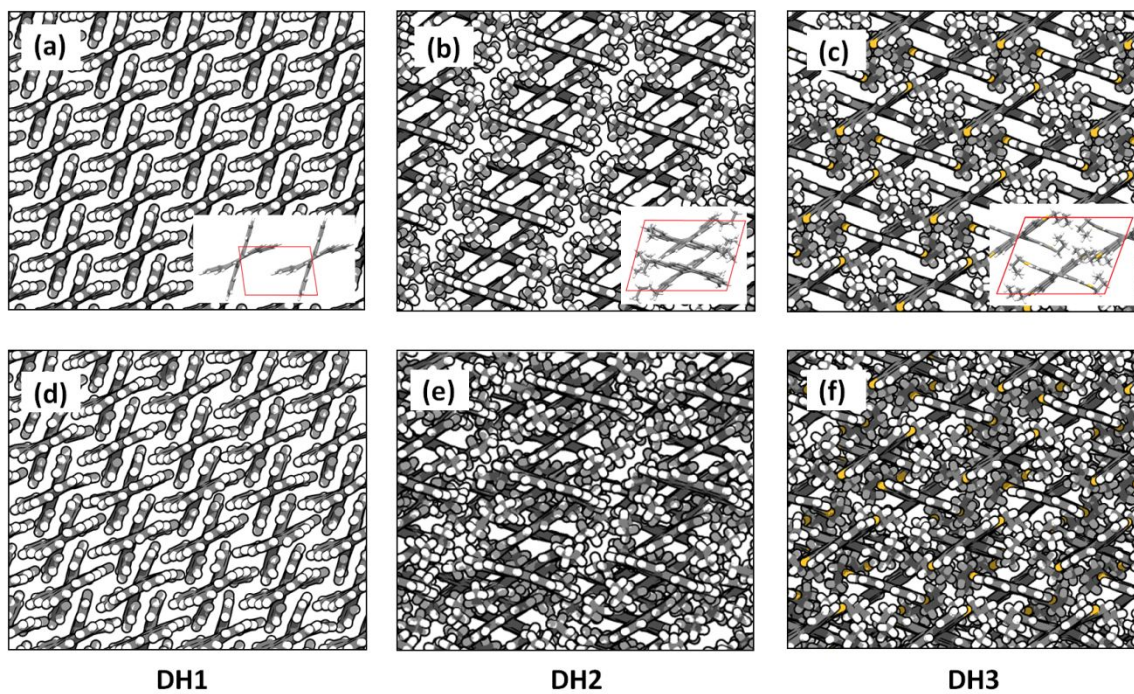
Figure 3. Ordered packing in supercells (a)-(c) and atomistic morphologies obtained from the snapshots of MD simulations at 300K (d)-(f). For each case, packing in one crystallographic layer is shown for clarity.

Room temperature MD simulations were performed to predict structural order in **DH1, DH2** and **DH3** in the solid state (Figure 3). We first calculated the unit cell parameters of **DH1**, **DH2** and **DH3** from the MD equilibrated supercells and found that the unit cells differ by 1.1%, 1.0% and 0.6% from the experimental unit cells, respectively. We suggest that the expansion of the unit-cell at room temperature is mainly responsible for the ~1% deviation, since (i) the xrd crystal structures are obtained at very low temperatures and (ii) the difference between the calculated and measured cell parameters are always positive for each crystallographic direction and each material. In order to quantify the effect of temperature on the structures, the RMSD between each MD-disordered systems and its initial experimental supercell was calculated from a single MD snapshot at 300K. The RMSD values of **DH1**, **DH2**, and **DH3** are 0.73 Å, 1.28 Å, and 0.56 Å, respectively. To account for the influence of *n*-butyl side-chains, the RMSD of **DH2** with the exclusion of alkyl side-chains was calculated and found to be 0.88 Å, a value still higher than but

closer to that of **DH1**. The average RMSD over individual molecules is ~0.2 Å for all **DHs**, indicating that the RMSD deviation can be largely attributed to relative orientations of the molecules and expansion of the supercells rather than changes in the DH molecules, highlighting the significance of the unique packing arrangements of the DHs.

We analyzed the dihedral angle between the π-blades in the XRD, DFT-optimized, and MD-disordered structures. The experimental dihedral angles between the π-blades of **DH1, DH2** and **DH3** are 41°, 50° and 53° respectively.[30] The dihedrals between the π-planes in the optimized structures are similar (46°, 49° and 47° for **DH1, DH2** and **DH3**, respectively) to the experimental values with deviations of 1-6°, suggesting that side-chains have a negligible effect on DH core structures. Dihedral angle distributions from MD simulations are shown in Figure 4a. The averages of these distributions are 42°, 49° and 54° for **DH1, DH2** and **DH3**, respectively, which are consistent with the values from XRD and DFT structures. To quantify structural disorder in these systems, we calculated the standard deviations of these dihedral angle distributions, which are found to be similar (3.8°, 3.4° and 4.6° for **DH1**, **DH2** and **DH3**, respectively).

In order to quantify the positional disorder between neighboring molecules, we calculated paracrystallinity along the strong π-π stacking directions. Paracrystallinity is defined as $g = s/\langle d \rangle$, where d is taken to be center-of-mass distances between neighboring molecules exhibiting strong π-π stacking, s is the standard deviation of an ensemble of d distances and $\langle \ldots \rangle$ represents an ensemble average.[69,70,71] A paracrystallinity value of ~0-1% corresponds to a nearly perfect order system, and a value of ~1-10% corresponds to disorder.[697] Paracrystallinity parameters for **DH1**, **DH2** and **DH3** are 1.7%, 2.2% and 1.3%, respectively, with **DH2** as the most structurally more disordered system and **DH3** least disordered, which is consistent with the RMSD analysis.

To summarize our characterizations of materials morphologies; our MD simulations reveal that the structural disorder of **DH2**, quantified by both RMSD and paracrystallinity, is higher than for **DH1**. In contrast, **DH3** has a smaller RMSD but disorder in the dihedral between the π-blades is larger. These observations cannot directly be attributed to the presence of side-chains since the presence of side-chains does not have strong influence on the ground state optimized structure. Thus, the relative positional disorder is largely caused by the difference in packing arrangement. However, as we will describe later,

large positional disorder does not necessarily bode poor charge transport in the

disordered phase.

III. 2. Charge Transport Parameters

In order to characterize the charge mobilities and probe the differences in charge

transport, we calculate a number of relevant parameters, including hole-transfer

reorganization energy, electronic coupling, and energetic disorder of **DH1, DH2** and **DH3**.

We compare the charge-transport parameters to those of pentacene and rubrene, high-

performing systems that were studied in our previous hole mobility benchmark.[33] The

reorganization energy λ is an intrinsic property of the system that quantifies energetic

changes due to structural variations between ground and excited state structures. We

use gas phase optimizations of **DHs** to calculate λ according to the four-point rule based

on the potential energy curves. Reorganization energies are very similar for **DH1, DH2**

and **DH3** (λ = 117, 122 and 108 meV, respectively), indicating that addition of side-chains

and/or heteroaromatic substitution has negligible influence on λ due to the inherently

similar core structures. However, there is correlation between the degree of twisting in

each π-blade and λ across the three structures. As discussed in the previous section, the

twisting in the π-blade is exhibited in the DFT-optimized structures but not in the crystal

structure (Figure 2). The twisting is smallest in **DH3** and largest in **DH2**, which are in line

with the calculated reorganization energies. These reorganization energies are also

comparable to those of pentacene (100 meV) and rubrene (160 meV), both of which have

shown highly efficient charge transport in organic semiconductors.

   To quantify the disorder energetically, in addition to structural disorder, we calculated

the variations in site-energy difference distributions in the equilibrated morphologies from

MD, which have often been used as measures of energetic disorder σ.[72,73,74,75] The width

of the site-energy difference distributions is similar for all **DHs** andthe width of the

distributions, *i.e.* energetic disorder, of **DH1** (50 meV), **DH2** (44 meV) and **DH3** (60 meV)

are also close (Figure 4b). Similarly, the σ values we found for **DHs** are close to those

previously calculated for pentacene and rubrene based on the same methodology (68

and 53 meV, respectively).[33] σ is also directly related to the local electron-photon coupling

(or reorganization energy) in organic materials and the similar σ results we found for DHs

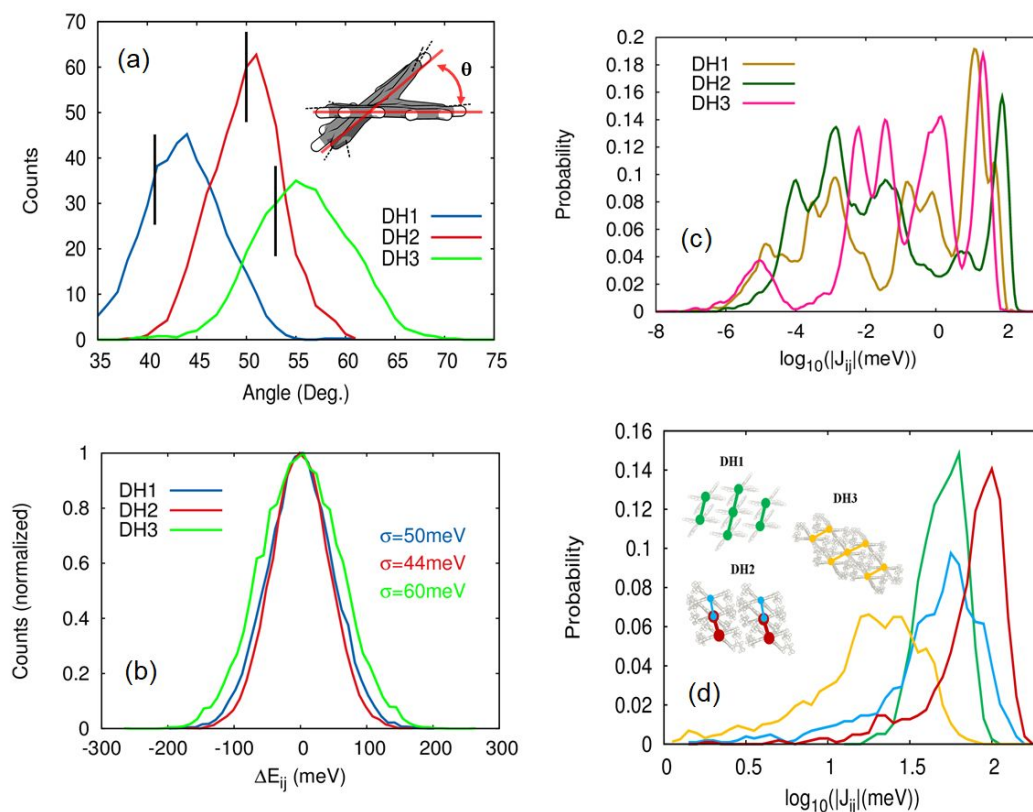qualitatively agree with their similar reorganization energies.[76]

Figure 4. (a) Distributions of the angles between the plane of two π-blades of **DH1, DH2** and **DH3**. The vertical black lines represent values obtained from XRD measurements. Inset: Representative schematic illustrating the angle between two π-blades of **DHs**, where dashed lines indicate the fused portion of the molecule not pictured. (b) Site-energy difference distributions of **DH1, DH2** and **DH3**. Standard deviations, *i.e.* energetic disorders, are indicated. Electronic coupling distributions of the (c) overall packing and (d) π-π stacking arrangements.

We then calculated the electronic coupling of the charge-transfer between neighboring molecules in ordered **DH1, DH2** and **DH3** using the DFT-based DIPRO and ZINDO-based

MOO methodologies (Figure 5). First, we see that the ZINDO electronic coupling results are typically very close to DFT. Electronic coupling in the π-π stacking direction are high for both **DH1** and **DH2**, while lower for **DH3**. Analysis of the geometrical parameters of the π-π stackings presented in Figure 5 revealed that, the significantly large interplanar overlap of the blades of **DH1** and **DH2**, as well as small interplanar distance of **DH2,** comparing with **DH3** is responsible for large electronic coupling of **DH1** and **DH2**. On the other hand, electronic coupling values in the π-π stacking direction of pentacene and rubrene are ~60 and 80 meV, respectively.[33] Similar to the λ values, J values of both **DH1** and **DH2** are comparable to high-mobility pentacene and rubrene and indicative of high charge-transport performance. Electronic coupling determines charge-transport propensity; charge transport occurs predominantly in one crystallographic direction for the ordered **DH1** and **DH3**, whereas charge transport alternates even in one crystallographic direction for the ordered **DH2** due to alternating electronic couplings, as shown in Figure 5.
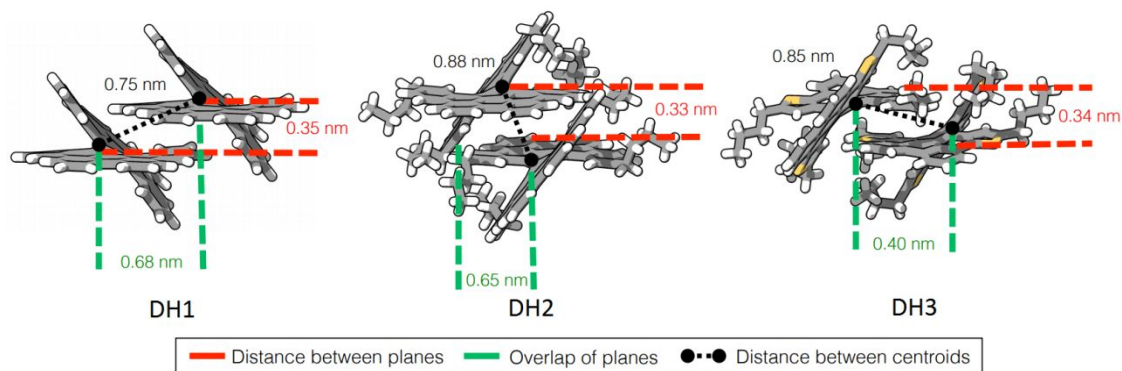
DH1

DH2

DH3

DFT/ZINDO

J (meV)

56/58

9/9

66/73

41/41

4/14

44/37
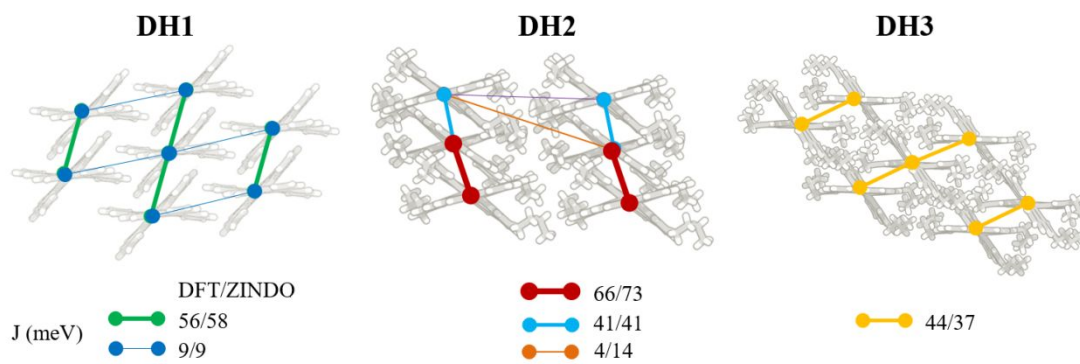
Figure 5. (top) Crystal packing motifs and strong transport pathways of **DH1**, **DH2**, and **DH3**. The connections correspond to intermolecular electronic coupling, J (in meV), calculated by both DFT (B3LYP/6-31G(d)) and ZINDO methodology. DFT *vs.* ZINDO results are shown as such: J(DFT)/J(ZINDO). Thickness of each line is coherent with the strength of the corresponding coupling. A J value of 39/38 meV in **DH3** along [110] direction (see Scheme 1) and the remaining weak J for all DHs values are not shown for clarity. (b) Geometrical parameters of strong DH pairs extracted from XRD crystal structures, corresponding to green, red, and yellow pathways for **DH1**, **DH2**, and **DH3**, respectively. Although it is not shown, distance between planes, overlap of planes and distance between centroids are 0.74, 0.81, 0.35 nm for the other strong pair of **DH2** (light blue pair in the top figure).

Analysis of the electronic coupling distribution of the disordered DH systems is shown in Figures 4c and 4d. Figure 4c shows the distribution of the overall electronic coupling in each of the systems, with peaks at various points due to multiple transport directions. There are two peaks in the strong electronic coupling region for **DH1**, corresponding to

$<J>$ = 10 meV and $<J>$ = 49 meV, which correspond to weak and strong π-π stacking in

DH1, since, as described earlier, the interaction energy of the former is -10 kcal/mol, while

that of the latter is -26 kcal/mol. For **DH2**, a combination of two couplings (49 and 75 meV)

forms a single peak; these are the J values of the two strong π-π stacking interactions of

DH2 having large geometrical overlap and interaction energies of -34 and -29 kcal/mol,

which coexist alternatively along the charge-transport direction discussed earlier in the

text. The maximum of the electronic-coupling distribution of **DH2** is higher than **DH1**,

consistent with J values in ordered morphologies. For **DH3**, coupling peaks at lower

values than those of **DH1** and **DH2**, with an average value of 21 meV and corresponding

to the π-π stacking of **DH3**. This value is considerably lower than electronic coupling value

obtained for **DH3** in the ordered phase (37 meV). Figure 4d shows direction-resolved

electronic coupling for the equilibrated atomistic morphologies. Electronic coupling

distributions in both π-π stacking directions in **DH2** (blue and red) are broader than the

one direction in **DH1** (green) and **DH3** (yellow). The standard deviation of each of these

peaks (Σ) is low for **DH1** and **DH3** (13 meV for each) but much higher for the two peaks

in **DH2** (26 and 29 meV). The broader J distribution in the π-π stacking of **DH2** is

attributed to the higher positional disorder, which arises from higher RMSD and

paracrystallinity values compared to the other two systems.

We analyzed the temporal evolution of the electronic coupling in order to determine (i)

the origin of disorder (static, on time scale of transport, or dynamic) we observe in our

equilibrated morphologies and (ii) non-local electron-phonon coupling, calculated from

$L = \delta J^2 / 2 k_B T$, where δJ is the width of the electronic-coupling distributions.[77] The time

scale of static disorder is usually longer than the time scale of charge transport and is

typically caused by the defects, impurities, irregularities etc., while the dynamic disorder

is caused by the thermal fluctuations, *i.e.* molecular vibrations. A direct comparison

between the time distributions and ensemble distributions would give clues about the

origin of disorder.[78] In Figure 6 (a), for selected pairs belonging to the pathways with

strongest coupling we see fine scale oscillations in electronic coupling and the amplitude

of the oscillations are found to be similar for **DH1** and **DH3**, but those of **DH2** are

significantly larger. The large amplitude of oscillations can be attributed to the strong

geometrical overlap in **DH2** (see Figure 5) of which translates into large restraining forces.

We then calculated the time distributions and ensemble distributions of electronic

coupling and saw that the width and positions of the distributions are similar for **DH1**, **DH2**

and **DH3**, as shown in Fig. 6 (b)-(d). This indicates that the thermal fluctuations are mainly

responsible for the disorder we observed in DHs. Calculation of the non-local electron-

photon coupling revealed that, for DH1 and **DH3**, L values are within 2-4 *meV* and are

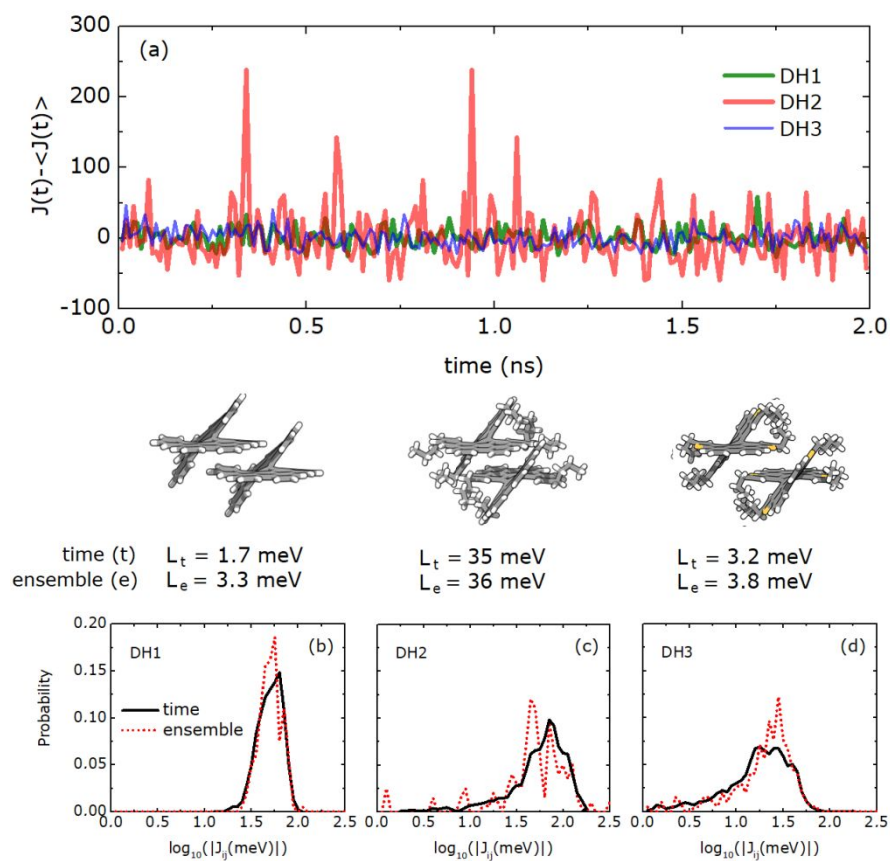negligibly small but L is significantly larger and found to be ~35meV.

Figure 6. (a) Temporal evolutions of electronic-coupling fluctuations, as J(t)-<J>, of the selected

pairs of DH1 (green line), DH2 (red line) and DH3 (blue line), where <…> represents the temporal

average. The graph shows only the first 2 *ns* of the MD simulation at 300K. (middle) Non-local electron-phonon coupling results calculated by the time and single-snapshot ensemble distributions shown in (b)-(d). The selected pairs correspond to the molecular packings of the strongest transport pathways.

III. 3. Mobility

Using the charge transport parameters calculated in the previous section, we calculated hole mobilities of the three molecules based on ordered and disordered morphologies. The summary of prominent charge-transport parameters along with the hole mobilities of **DH1, DH2** and **DH3** are given in Table 1. We compare our results against those of high-mobility pentacene and rubrene, where the parameters were calculated using the same method in ref. 33. We first calculated hole mobilities from the unit cells, *i.e.* hypothetically perfect order was considered (*i.e.* g = 0, σ = 0). As discussed earlier, reorganization energies of all systems are similar and the electronic coupling of **DH1** and **DH3** is weaker than **DH2**; however, the predicted hole mobility of **DH1** (8.6 cm^2/Vs based on ZINDO and 10.1 cm^2/Vs based on DFT) is higher than that of **DH2** (5.7 cm^2/Vs and 4.3 cm^2/Vs), which is surprising since the charge-transfer rate is proportional to J^2. In **DH1**, charge transfer

is confined to a single direction, while the transfer travels in two directions for **DH2**, as well as alternating packing in the $\pi-\pi$ stacking direction is observed for **DH2** due to chirality (see Figure 5). In a defect-free crystal, an alternating pattern in charge transport results in a decrease in the charge-carrier's net velocity, which is related to the lower hole mobility. If a charge-carrier is formed in a hopping site where transfer to the surrounding sites is unfavorable, the probability for the carrier to oscillate in the site and remain stagnant increases, causing an overall decrease in hole mobility. Therefore, for these systems, heterochiral transport is less favorable than homochiral transport in an ordered phase. The hole mobility of **DH3** is lower than **DH1** but same as **DH2**, which is, in our case, expected considering the lower J values for the homochiral transport.
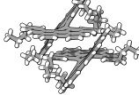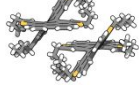
The situation is dramatically different for the case of disordered morphologies. Starting supercells were equilibrated using MD simulations, resulting in slight positional disorder. As expected, the added positional and energetic disorder results in decreased hole mobilities. While the hole mobility of **DH1** decreases roughly by a factor of four relative to its ordered hole mobility, the hole mobility of **DH2** is only slightly affected by disorder. Moreover, while the ordered hole mobility of **DH2** is the lowest of all molecules in Table

1, the disordered hole mobility is the highest, close to its value in the ordered phase. With

disorder, the hole-mobility of **DH3** decreases more than an order of magnitude from 5.7

to 0.4 cm^2 V^{-1} s^{-1}. Fujikawa *et al.*[31] obtained the experimental hole-mobility of **DH3** in an

OFET configuration and obtained a value of 0.033 cm^2/Vs, which is nearly an order of

magnitude lower than our prediction. As the experimental mobility has not been

optimized,[79] the discrepancy between our prediction and the experimental results can be

attributed to the polycrystalline nature of the thin-film transistor, which creates grain

boundaries that impair charge-transport. Futhermore, a direct quantitative comparison

between the experimental measurement and theoretical prediction for an organic

semiconductor is still challenging for few other reasons. First, the OFET devices possess

a complex configuration at which the organic semiconductor lies on an inorganic dielectric

material and is in contact with source, drain and gate electrodes, each of which is

distinctively effecting the performance of the device and causes difficulties in extracting

intrinsic mobilities. Second, in some situations the molecular packing motifs are being

different in crystals than in disordered thin films which rules out direct comparison with

the experiments. Third, the organic semiconductor mobilities extracted from current-

voltage measurements is based on oversimplified device models which are recently being questioned intensively.[80]   Thus, we believe our value of 0.4 cm^2 V^{-1} s^{-1} for **DH3** is the theoretical upper limit for mobility that could be reached   upon optimization of device processing. [54,78] We make mention that the experimental mobilities of DH1 and DH2 have not been achieved yet and thus no comparisons can be made.[79]

   We further used the transient localization model to obtain hole mobilities for comparision (see Supporting Information). Using the average electronic coupling values, we predicted the localization lengths of **DH1**, **DH2** and **DH3**. Correspondingly, the mobilities of these compounds are predicted to be 6.2, 14.4 and 2.5 cm^2 V^{-1} s^{-1} for **DH1**, **DH2** and **DH3**, respectively. The mobilities are systematically larger than those predicted by the rate-based model; the mobilities of **DH1** and **DH2** are roughly by a factor of three larger but that of **DH3** is a factor of six larger. The ordering of mobilities **DH2** > **DH1** > **DH3** found by this method is consistent with the rate-based model.

Table 1. Summary of charge-transport parameters for DH1, DH2 and DH3 and comparisons with benchmark materials; pentacene and rubrene.

	Ordered					Disordered				
	λ	$J_{\pi-\pi}$ (DFT)	$J_{\pi-\pi}$ (ZINDO)	μ (DFT)	μ (ZINDO)	g	$\langle J_{\pi-\pi}\rangle$	σ	μ	μ_{exp}
DH1	117	56	58	10.1	8.6	1.7	49	50	2.3	n/a
DH2	122	66	73	4.3	5.7	2.2	75	44	5.1	n/a
DH3	108	44	37	6.9	5.7	1.3	21	60	0.4	0.033[a]
pentacene*	95	42[§]	61	10.4	15.6	2.5	32	68	0.7	1.45[b]
rubrene*	160	106[§]	81	20.3	11.6	1.5	75	53	1.9	8.6[b]

Reorganization energy, λ, electronic-coupling, J, and energetic disorder, σ, are in units of meV. Paracrystallinity parameter, g, is % and hole-mobility, μ, is in units of cm²/Vs. The average electronic coupling results (and, consequently, the hole mobilities) for disordered morphologies are calculated by ZINDO. [a] ref. 31, [b] ref. 60. *Reorganization energies and ZINDO calculations of pentacene and rubrene are taken from ref. 33, DFT based electronic coupling and mobilities are our work. [§]DFT calculated electronic coupling for the remaining directions were calculated to be 56 and 89 meV for pentacene and 18 meV for rubrene in ref. 33.

In order to understand the disproportionate changes in the predicted disordered hole

mobilities due to the presence of disorder, we plotted connectivity graphs showing the

transport networks in a single MD snapshot (Figure 7). The center-of-masses of the

molecules are represented by spheres and strong electronic couplings between these

sites (where $J > 20$ meV) are represented by the red lines. For **DH1**, strong coupling

occurs along the [001] direction (with some in the (110) plane), which results in mainly one-dimensional transport, *i.e.*, charge transport predominantly occurs in only one crystallographic direction. On the other hand, there are two strong electronic couplings in **DH2**, which are along the [100] and [010] crystallographic directions. This, on the other hand, results in a two-dimensional transport network in **DH2**. Even though coupling is especially strong along one direction in **DH1** (<J> = 46±13 *meV*), the system is sensitive to charge-trapping due to positional disorder, which results in the hole mobility decreasing by a factor of 4 with the introduction of disorder ($\mu_{ideal} = 8.6$ to $\mu_{disor} = 2.3$ cm^2/Vs). On the other hand, the hole mobility of **DH2** is nearly maintained in the presence of disorder, as trap states can be bypassed due to the two-dimensional nature the transport network in this system. In general, electronic coupling in the **DH3** system is lower than in the other two systems. For **DH3**, we do not observe many connections due to weak electronic coupling values (<20 meV), which impair charge transport and leads to traps. Moreover, the connectivity seems to be three-dimensional which is known to be destructive for charge-transport.[31] As a result, the mobility of **DH3** decreases from 5.7 to 0.4 cm^2/Vs, corresponding to a nearly 15-fold decrease in mobility.

Although the diverse connectivity in an ordered **DH2** is unfavorable for charge-transport,

it becomes beneficial in its disordered morphology for achieving high-mobility, as a

charge-carrier can easily bypass a trap-state by following other favorable pathways. In

disordered morphologies, having diverse pathways is favorable due to the increased

probability of a charge carrier being able to bypass charge traps. Our findings are in line

with previous studies on conjugated organic polymers. Noriega *et al.*[33] showed that the

requirement for high mobility in conjugated polymers was the presence of interconnected

aggregates rather than an increase in crystallinity. Molecular dynamics simulations by

Jackson et al.[81] also indicate that conformationally disordered polymers can still result in

efficient devices due to the ability of the polymers to form local molecular ordering, which

is of higher importance than long-range crystallinity. Similarly, although disordered **DH2**

shows high positional disorder, its ability to form interconnected hopping sites allow for

high mobility despite disorder. **DH2** is a promising disordered organic material and

potentially may have one of the highest hole mobilities as an organic semiconductor that

can readily be implemented in both single crystal and thin film technology. Our results are

in line with previous examples of side-chain engineering as a means to control solid-state

packing and therefore tune dimensional charge transport.[82] In particular, Tsutsui and coworkers engineered different packing arrangements (either 1D or 2D) of benzothienobenzothiophenes (BTBTs) by changing the position of alkyl group functionalization.[82d] As a result, the group achieved one of the highest organic crystal mobilities reported for organic crystals, 170 cm^2 V^{-1} s^{-1}. Using computations, we demonstrate that alteration of the packing of this class of helicenes can be achieved with side-chain manipulation, giving rise to the potential for high mobility in both ordered and disordered morphologies.
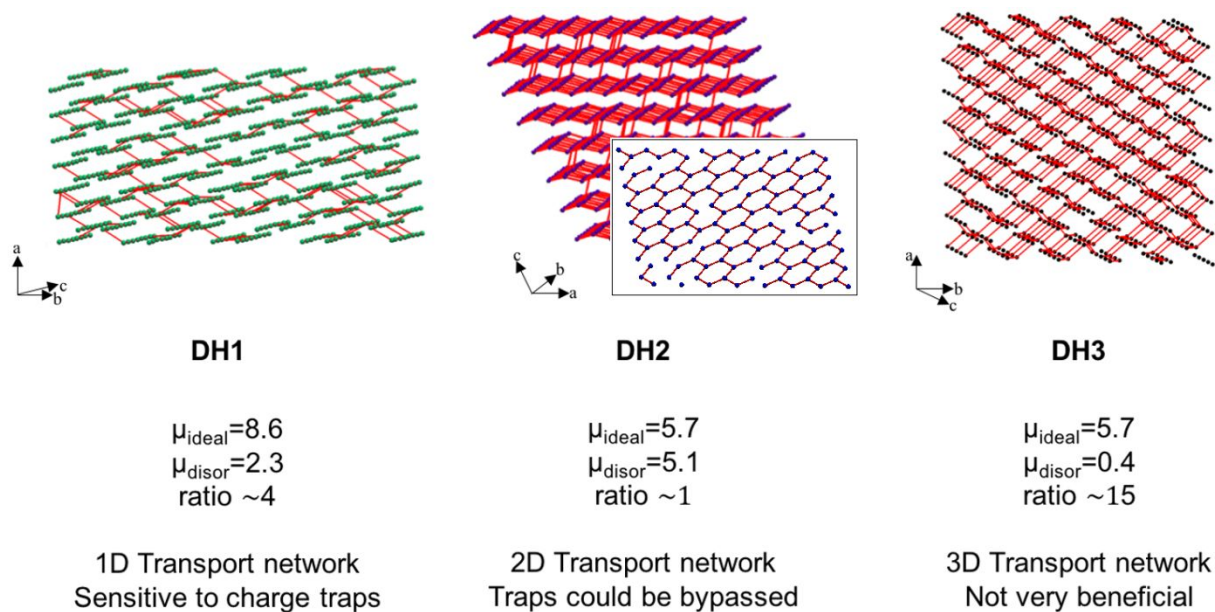

DH1	**DH2**	**DH3**
μ_{ideal}=8.6	μ_{ideal}=5.7	μ_{ideal}=5.7
μ_{disor}=2.3	μ_{disor}=5.1	μ_{disor}=0.4
ratio ~4	ratio ~1	ratio ~15
1D Transport network	2D Transport network	3D Transport network
Sensitive to charge traps	Traps could be bypassed	Not very beneficial

Figure 7. Connectivity graphs showing the transport networks of disordered **DH1, DH2** and **DH3**. Green, blue and and black dots indicate central of masses of molecules and connections (red) represent electronic coupling values (where J > 20 meV) between neighboring pairs. For DH2, the inset shows the top view of a selected (001) plane. Mobilities are in units of cm^2 V^{-1} s^{-1}.

IV. Conclusions

Atomistic morphologies and charge transport of unsubstituted and substituted π-extended double helicenes (**DH1** and **DH2**) and of a thiophene variant (**DH3**) are predicted. In the solid-state, each material exhibits a unique form of contorted packing and comprise both homochiral and heterochiral packing in the crystal structure. Using MD simulations, we examine the distributions of dihedral angles of π-blades and calculate RMSD and paracrystallinity parameters in order to quantify structural disorder and understand the atomistic morphologies in the solid state. Our results reveal that **DH2** morphology is structurally more disordered compared to **DH1** and **DH3**. We then perform

charge-transport simulations and calculated reorganization energies, electronic coupling and hole mobilities. The reorganization energies are similar, but the electronic coupling between π-π stacked neighboring pairs are different and highly dependent on the relative orientations of the DH molecules. Electronic coupling of DH2 is stronger than that of DH1 or DH3. These results reveal that, despite the dramatic influence on the packing arrangement, side-chain substitution has no direct impact on bulk features. Hole mobilities of DH1, DH2, and DH3 were predicted based on ordered and disordered morphologies, using kinetic Monte Carlo simulation methods. The hole mobility of ordered DH2 is lower than for DH1, although the electronic coupling of DH2 is stronger. This discrepancy is attributed to the alternating transport network of DH2 crystal due to heterochirality in the $\pi-\pi$ stacking direction, which makes the system vulnerable to shallow charge-traps, even in an ordered morphology. DH3 also comprises a somewhat three-dimensional transport network, but we observe that it is not beneficial for charge transport. We then predict hole mobilities in the disordered morphologies, in which positional and energetic disorders is present. We find that the hole mobility of DH2 is markedly higher than DH1, DH3, and benchmark high-mobility organic semiconductors

rubrene and pentacene. Examination of electronic coupling within the disordered system reveals that even in the presence of disorder, there exists favorable transport pathways. The 2D transport network in **DH2**, in which the system is susceptible to charge-trapping in ordered morphology, is favorable in disordered morphologies due to increased probability of bypassing charge trap states. Moreover, roughly an order of magnitude stronger non-local electron-phonon coupling found in **DH2** comparing with **DH1** and **DH3** suggests that the large dynamic disorder in **DH2** caused by the thermal fluctuations is compensated by the dimensionality of the transport.

Our results point to an important notion that in rationally designing *intrinsically* high mobility organic semiconductors, packing arrangements and the resulting charge transport networks in the solid-state is as important as (and in our case more important than) the molecular architecture and solid-state order. However, *a priori* knowledge of crystal packing and transport network for a given material remains elusive, but designing a high profile material typically rely on the potential of the reported results of a similar material. Our results showed that with a rigorous control over the disorder and packing

arrangement, mobilities on the order of 10 cm^2/Vs can be achieved from double-helicenes. Therefore, this work provides fundamental understanding of the differences in charge transport in single crystal and thin film morphologies and serves as a foundation for understanding of other materials with multi-dimensional charge transport.

ASSOCIATED CONTENT

Supporting Information. DFT optimized geometries, partial charges, MD snapshots at different crystallographic directions and details of the electronic coupling calculations can be found in the Supporting Information.

AUTHOR INFORMATION

The authors declare no competing financial interests.

ACKNOWLEDGMENT

REFERENCES

———————————

[1] Ostroverkhova, O. Organic Optoelectronic Materials: Mechanisms and Applications. *Chem. Rev.* 2016, **116**, 13279-13412.

[2] Wang, C. Dong, H. Jiang L. and Hu, W. Organic Semiconductor Crystals. *Chem. Soc. Rev.*, 2018, **47**, 422-500.

[3] Yao, Z.-F. Wang, J.-Y. and Pei, J. Control of π-π Stacking via Crystal Engineering in Organic

Conjugated Small Molecule Crystals *Cryst. Growth Des.* 2018, **18**, 7-15.

[4] For a review of contorted aromatics, see: Ball, M. Zhong, Y. Wu, Y. Schenck, C. Ng, F. Steigerwald, M. Xiao, S. and Nuckolls, C. Contorted Polycyclic Aromatics. *Acc. Chem. Res.* 2015, **48**, 267-276.

[5] Ball, M. Zhong, Y. Fowler, B. Zhang, B. Li, P. Etkin, G. Paley, D. W. Decatur, J. Dalsania, A. K. Li, H. Xiao, S. Ng, F. Steigerwald, M. L. and Nuckolls, C. Macrocyclization in the Design of Organic n-Type Electronic Materials. *J. Am. Chem. Soc.* 2016, **138**, 12861-12867.

[6] Schuster, N. J. Paley, D. W. Jockusch, S. Ng, F. Steigerwald, M. L. and Nuckolls, C. Electron Delocalization in Perylene Diimide Helicenes. *Angew. Chem. Int. Ed.* 2016, **55**, 13519-13523.

7 Sisto, T. J. Zhong, Y. Zhang, B. Trinh, M. T. Miyata, K. Zhong, X. Zhu, X.-Y. Steigerwald, M. L. Ng, F. and Nuckolls, C. Long, Atomically Precise Donor—Acceptor Cove-Edge Nanoribbons as Electron Acceptors. *J. Am. Chem. Soc.* 2017, **139**, 5648-5651.

8 For work on helical nanoribbon photodetectors, see: Zhong, Y. Sisto, T. J. Zhang, B. Miyata, K. Zhu, X.-Y. Steigerwald, M. L. Ng, F. and Nuckolls, C. Helical Nanoribbons for Ultra-Narrowband Photodetectors. *J. Am. Chem. Soc.* 2017, **139**, 5644-5647.

9 For work by Nuckolls on using contorted hexabenzocoronenes in OFETs, see: Cohen, Y. S. Xiao, S. Steigerwald, M. L. Nuckolls, C. and Kagan, C. R. Enforced One-Dimensional Photoconductivity in Core-Cladding Hexabenzocoronenes. *Nano Lett.* 2006, **6**, 2838-2841.

10 Skabara, P. J. Arlin, J.-B. and Geerts, Y. H. Close Encounters of the 3D Kind − Exploiting High Dimensionality in Molecular Semiconductors. *Adv. Mater.* 2013, **25**, 1948-1954.

11 Arumugam, S. Wright, I. A. Inigo, A. R. Gambino, S. Howells, C. T. Kanibolotsky, A. L. Skabara, P. J. and Samuel, I. D. W. Charge Transport in a Two-Dimensional Molecular Organic Semiconductor. *J. Mater. Chem. C* 2014, **2**, 34-39.

[12] Calvo-Castro, J. Morris, G. Kennedy, A. R. and McHugh, C. J. Fluorine Directed Two-Dimensional Cruciform π−π Stacking in Diketopyrrolopyrroles. *Cryst. Growth Des.* 2016, **16**, 5385-5393.

[13] For a review of synthesis and applications of helicenes, see: Shen, Y. and Chen, C.-F. Helicenes: Synthesis & Applications. *Chem. Rev.* 2012, **112**, 1463-1535.

[14] Kang, S. J. Ahn, S. Kim, J. B. Schenck, C. Hiszpanski, A. M. Oh, S. Schiros, T. Loo, Y.-L. and Nuckolls, C. Using Self-Organization to Control Morphology in Molecular Photovoltaics. *J. Am. Chem. Soc.* 2013, **135**, 2207-2212.

[15] Schiros, T. Kladnik, G. Prezzi, D. Ferretti, A. Olivieri, G. Cossaro, A. Floreano, L. Verdini, A. Schenck, C. Cox, M. Gorodetsky, A. A. Plunkett, K. Delongchamp, D. Nuckolls, C. Morgante, A. Cvetko, D. and Kymissis, I. Donor—Acceptor Shape Matching Drives Performance in Photovoltaics. *Adv. Energy Mater.* 2013, **3**, 894-902.

[16] Rice, B. LeBlanc, L. M. Otero-de-la-Roza, A. Fuchter, M. J. Johnson, E. R. Nelson, J. and Jelfs, K. E. A Computational Exploration of the Crystal Energy and Charge-Carrier Mobility Landscapes of the Chiral [6] Helicene Molecule. *Nanoscale* 2018, **10**, 1865-1876.

[17] Zoppi, L. Martin-Samos, L. and Baldridge, K. K. Effect of Molecular Packing on Corannulene-Based Materials Electroluminescence. *J. Am. Chem. Soc.* 2011, **133**, 14002-14009.

[18] Xiao, S. Myers, M. Miao, Q. Sanaur, S. Pang, K. Steigerwald, M. L. and Nuckolls, C. Molecular Wires from Contorted Aromatic Compounds. *Angew. Chem., Int. Ed.* 2005, **44**, 7390-7394.

[19] For select example of contorted aromatics in solar cells, see: Kang, S. J. Kim, J. B. Chiu, C.-Y. Ahn, S. Schiros, T. Lee, S. S. Yager, K. G. Toney, M. F. Loo, Y.-L. and Nuckolls, C. A Supramolecular Complex in Small-Molecule Solar Cells based on Contorted Aromatic Molecules. *Angew. Chem., Int. Ed.* 2012, **51**, 8594-8597.

[20] For select example of contorted aromatics in thin-film transistors, see: Xiao, S. Kang, S. J. Zhong, Y. Zhang, S. Scott, A. M. Moscatelli, A. Turro, N. J. Steigerwald, M. L. Li, H. and Nuckolls, C. Controlled Doping in Thin-Film Transistors of Large Contorted Aromatic Compounds. *Angew. Chem., Int. Ed.* 2013, **52**, 4558-4562.

[21] For select example of tunability of contorted aromatics, see: Li, Y. Jia, Z. Xiao, S. Liu, H. and Li, Y. A Method for Controlling the Synthesis of Stable Twisted Two-Dimensional Conjugated Molecules. *Nat. Commun.* 2015, **7**, 11637-11647.

[22] For early work on the development of Spiro-OMeTAD, see: Salbeck, J. Yu, N. Bauer, J. Weissörtel, F. and Bestgen, H. Low Molecular Organic Glasses for Blue Electroluminscence. *Synth. Met.* 1997, **91**, 209-215.

[23] For experimental work on the crystal structure and hole transport of Spiro-OMeTAD, see: Shi, D. Qin, X. Li, Y. He, Y. Zhong, C. Pan, J. Dong, H. Xu, W. Li, T. Hu, W. Brédas, J.-L. and Bakr, O. M. Spiro-OMeTAD Single Crystals: Remarkably Enhanced Charge-Carrier Transport via Mesoscale Ordering. *Sci. Adv.* 2016, **2**, e1501491.

[24] For calculations of hole transport of Spiro-OMeTAD, see: Yavuz, I. and Houk, K. N. Mesoscale Ordering and Charge-Transport of Crystalline Spiro-OMeTAD Organic Semiconductors. *J. Phys. Chem. C*, 2017, **121**, 993-999.

[25] For pioneering work on the application of Spiro-OMeTAD in dye-sensitized solar cells, see: Bach, U. Lupo, D. Comte, P. Moser, J. E. Weissörtel, F. Salbeck, J. Spreitzer, H. and Grätzel, M. Solid-State Dye-Sensitized Mesoporous TiO_2 Solar Cells with High Photon-to-Electron Conversion Efficiencies. Nature 1998, **395**, 583-585.

[26] For a recent example on the application of Spiro-OMeTAD in dye-sensitized solar cells, see: Jang, S.-R. Zhu, K. Ko, M. J. Kim, K. Kim, C. Park, N.-G. and Frank, A. J. Voltage-Enhancement Mechanisms of an Organic Dye in High Open-Circuit Voltage Solid-State Dye-Sensitized Solar Cells. *ACS Nano* 2011, **5**, 8267-8274.

[27] For early work on the application of Spiro-OMeTAD in perovskite solar cells, see: Kim, H.-S. Lee, C.-R. Im, J.-H. Lee, K.-B. Moehl, T. Marchioro, A. Moon, S.-J. Humphry-Baker, R. Yum, J.-H. Moser, J. E. Grätzel, M. and Park, N.-G. Lead Iodide Perovskite Sensitized All-Solid-State Submicron Thin Film Mesoscopic Solar Cell with Efficiency Exceeding 9%. *Sci. Rep.* 2012, **2**, 591.

[28] For early work on the application of Spiro-OMeTAD in perovskite solar cells, see: Burschka, J; Pellet, N; Moon, S.-J. Humphry-Baker, R. Gao, P. Nazeeruddin, M. K. and Grätzel, M. Sequential Deposition as a Route to High-Performance Perovskite-Sensitized Solar Cells. *Nature* 2013, **499**, 316-319.

[29] For a recent review of Spiro-OMeTAD as a hole transport material in perovskite solar cells, see: Hawash, Z. Ono, L. K. and Qi, Y. Recent Advances in Spiro-MeOTAD Hole Transport Material and Its Applications in Organic–Inorganic Halide Perovskite Solar Cells. *Adv. Mater.* Interfaces 2017, 1700623.

[30] Fujikawa, T. Segawa, Y. and Itami, K. Synthesis, Structures, and Properties of π-Extended Double Helicene: A Combination of Planar and Nonplanar π-Systems. *J. Am. Chem. Soc.* 2015, **137**, 7763-7768.

[31] Fujikawa, T. Mitoma, N. Wakamiya, A. Saeki, A. Segawa, Y. and Itami, K. Synthesis, Properties, and Crystal Structure of π-Extended Double [6]Helicenes: Contorted Multi-Dimensional Stacking Lattice. *Org. Biomol. Chem.* 2017, **15**, 4697-4703.

[32] Kiel, G. R. Patel, S. C., Smith, P. W. Levine, D. S. and Tilley, T. D. Expanded Helicenes: A General Synthetic Strategy and Remarkable Supramolecular and Solid-State Behavior, *J. Am. Chem. Soc.* 2017, **139**, 18456-18459.

[33] Yavuz, I. Martin, B. N. Park, J. and Houk, K. N. Theoretical Study of the Molecular Ordering, Paracrystallinity, And Charge Mobilities of Oligomers in Different Crystalline Phases. *J. Am. Chem. Soc.* 2015, **137**, 2856-2866, and references therein.

[34] Ruehle, V. Lukyanov, A. May, F. Schrader, M. Vehoff, T. Kirkpatrick, J. Baumeier, B. and Andrienko, D. Microscopic Simulations of Charge Transport in Disordered Organic Semiconductors. *J. Chem. Theory Comput.* 2011, **7**, 3335-3345.

[35] Yavuz, I. Lopez, S. A. Lin, J. B. and Houk, K. N. Quantitative Prediction of Morphology and Electron Transport in Crystal and Disordered Organic Semiconductors. *J. Mater. Chem. C* 2016, **4**, 11238−11243.

[36] Case, D. A. *et al.* AMBER 12; University of California: San Francisco, CA, 2012.

[37] Salomon-Ferrer, R. Götz, A. W. Poole, D. Le Grand, S. and Walker, R. C. Routine Microsecond Molecular Dynamics Simulations with AMBER on GPUs. 2. Explicit Solvent Particle Mesh Ewald. *J. Chem. Theory Comput.* 2013, **9**, 3878-3888.

[38] Bayly, C. I. Cieplak, P. Cornell, W. and Kollman, P. A. A Well-Behaved Electrostatic Potential Based Method Using Charge Restraints for Deriving Atomic Charges: The RESP Model. *J. Phys. Chem.* 1993, **97**, 10269-10280.

[39] Wang, J. Wolf, R. M. Caldwell, J. W. Kollman, P. A. and Case, D. A. J. Development and Testing of a General Amber Force Field. *Comput. Chem.* 2004, **25**, 1157-1174.

[40] Nemkevich, A.; Buergi, H.-B.; Spackman, M. A.; Corry, B. Molecular dynamics simulations of structure and dynamics of organic molecular crystals *Phys.Chem. Chem. Phys.* 2010, **12**, 14916.

[41] Singh, U. C. and Kollman, P. A. An Approach to Computing Electrostatic Charges for Molecules. J. *Comput. Chem.* 1984, **5**, 129-145.

[42] Besler, B. H. Merz, K. M. and Kollman, P. A. Atomic Charges Derived from Semiempirical Methods. J. *Comput. Chem.* 1990, **11**, 431-439.

[43] Frisch, M. J. Trucks, G. W. Schlegel, H. B. Scuseria, G. E. Robb, M. A. Cheeseman, J. R. Scalmani, G. Barone, V. Mennucci, B. Petersson, G. A. Nakatsuji, H. Caricato, M. Li, X. Hratchian, H. P. Izmaylov, A. F. Bloino, J. Zheng, G. Sonnenberg, J. L. Hada, M.

Ehara, M. Toyota, K. Fukuda, R. Hasegawa, J. Ishida, M. Nakajima, T. Honda, Y. Kitao,

O. Nakai, H. Vreven, T. Montgomery, J. A., Jr. Peralta, J. E. Ogliaro, F. Bearpark, M.

Heyd, J. J. Brothers, E. Kudin, K. N. Staroverov, V. N. Kobayashi, R. Normand, J.

Raghavachari, K. Rendell, A. Burant, J. C. Iyengar, S. S. Tomasi, J. Cossi, M. Rega, N.

Millam, M. J. Klene, M. Knox, J. E. Cross, J. B. Bakken, V. Adamo, C. Jaramillo, J.

Gomperts, R. Stratmann, R. E. Yazyev, O. Austin, A. J. Cammi, R. Pomelli, C. Ochterski,

J. W. Martin, R. L. Morokuma, K. Zakrzewski, V. G. Voth, G. A. Salvador, P. Dannenberg,

J. J. Dapprich, S. Daniels, A. D. Farkas, Ö. Foresman, J. B. Ortiz, J. V. Cioslowski, J. and

Fox, D. J. Gaussian 09, Revision D.01; Gaussian Inc: Wallingford, CT, 2009.

[44] Allen, M. P. and Tildesley, D. J. Computer Simulation of Liquids; Oxford University

Press: Oxford, U.K., 1989.

[45] Stafström, S. Electron Localization and the Transition from Adiabatic to Nonadiabatic

Charge Transport in Organic Conductors. *Chem. Soc. Rev.* 2010, **39**, 2484-2499.

[46] Troisi, A. Charge Transport in High Mobility Molecular Semiconductors: Classic

Models and New Theories. *Chem. Soc. Rev.* 2011, **40**, 2347-2358.

[47] Kirkpatrick, J. An Approximate Method for Calculating Transfer Integrals Based on

the ZINDO Hamiltonian. *Int. J. Quantum Chem.* 2008, **108**, 51-56.

[48] Baumeier, B. Kirkpatrick, J. and Andrienko, D. Density-functional based determination of intermolecular charge transfer properties for large-scale morphologies. *Phys. Chem. Chem. Phys.*, 2010, **12**, 11103-11113.

[49] Brédas, J.- L. Calbert, J. P. da Silva Filho, D. A. and Cornil, J. Organic Semiconductors: A Theoretical Characterization of the Basic Parameters Governing Charge Transport. *Proc. Natl. Acad. Sci.* 2002, **99**, 5804-5809.

[50] Biancardi, A.; Caricato, M. A Benchmark Study of Electronic Couplings in Donor–Bridge–Acceptor Systems with the FMR-B Method *J. Chem. Theory Comput.* 2018, **14**, 2007−2016.

[51] Grimme, S. Semiempirical GGA-type density functional constructed with a long-range dispersion correction. *J. Comput. Chem.* 2006, **27**, 1787−1799.

[52] Coropceanu, V. Cornil, J. da Silva Filho, D. A. Olivier, Y. Silbey, R. and Brédas, J.-L. Charge Transport in Organic Semiconductors. *Chem. Rev.* 2007, **107**, 926-952.

[53] Bässler, H. Charge Transport in Disordered Organic Photoconductors: A Monte Carlo Simulation Study. *Phys. Status Solidi* (B) 1993, **175**, 15-56.

[54] Sokolov, A. N. Atahan-Evrenk, S. Mondal, R. Akkerman, H. B. Sánchez-Carrera, R. S. Granados-Focil, S. Schrier, J. Mannsfeld S. C. B. Zoombelt A. Bao Z. and Aspuru-

Guzik, A. From computational discovery to experimental characterization of a high hole mobility organic crystal. *Nature Comm.,* 2011, **2**, 437.

55 Oberhofer, H. Reuter, and K. Blumberger, J. Charge Transport in Molecular Materials: An Assessment of Computational Methods. *Chem. Rev.* 2017, **117**, 10319−10357.

56 Park, J. W. Lee, K. I. Choi, Y.-S. ; Kim, J.-H. Jeong, D. Kwon, Y.-N. Park, J.-B. Ahn, H. Y. Park J.-I. Lee H. S. and Shin J. The Prediction of Hole Mobility in Organic Semiconductors and Its Calibration Based on the Grain-Boundary Effect. *Phys. Chem. Chem. Phys*., 2016, **18**, 21371-21380.

57 Yavuz, I. Dichotomy Between the Band and Hopping Transport in Organic Crystals: Insights from Experiments. *Phys. Chem. Chem. Phys.* 2017, **19**, 25819-25828.

58 Yavuz, I. Lopez, S. A. Lin, J. B. and Houk, K. N. Quantitative Prediction of Morphology and Electron Transport in Crystal and Disordered Organic Semiconductors. *J. Mater. Chem. C* 2016, **4**, 11238−11243.

59 Shuai, Z. Geng, H. Xu, W. Liao, Y. and Andre, J.-M. From Charge Transport Parameters to Charge Mobility in Organic Semiconductors through Multiscale Simulation. *Chem. Soc. Rev.* 2014, **43**, 2662−2679.

60 Troisi, A. Charge Transport in High Mobility Molecular Semiconductors: Classical Models and New Theories. *Chem. Soc. Rev.* 2011, **40**, 2347–2358.

[61] Liu, C. Huang, K. Park, W. T. Li, M. Yang, T. Liu, X. Liang, L. Minari T. and Noh, Y. Y. A Unified Understanding of Charge Transport in Organic Semiconductors: The Importance of Attenuated Delocalization for the Carriers. *Mater. Horiz.*, 2017, **4**, 608-618.

[62] Fratini, S. Ciuchi, S. Mayou, D. Trambly de Laissardière, G. and Troisi, A. A Map of High-Mobility Molecular Semiconductors. *Nature Mat.* 2017, **16**, 998-1002.

[63] Bastiansen, O. The Molecular Structure of Biphenyl and Some of Its Derivatives. *Acta Chem. Scand.* 1949, **3**, 408-414.

[64] Takayanagi, M. Gejo, T. and Hanazaki, I. Geometry and Torsional Potential of 2,2'-Bithiophene in a Supersonic Jet. *J. Phys. Chem.* 1994, **98**, 12893-12898.

[65] Pelletier, M. and Brisse, F. Bithiophene at 133 K. *Acta Cryst.* C 1994, **50**, 1942-1945.

[66] Chaloner, P. A. Gunatunga, S. R. and Hitchvock, P. B. Redetermination of 2,2'-Bithiophene. *Acta Cryst.* C 1994, **50**, 1941-1942.

[67] Siegrist, T. Kloc, C. Laudise, R. A. Katz, H. E. and Haddon, R. C. Crystal Growth, Structure, and Electronic Band Structure of α-4T Polymorphs. *Adv. Mater.* 1998, **10**, 379-382.

[68] Vujanovich, E. C. Bloom, J. W. G. and Wheeler, S. E. Impact of Neighboring Chains on Torsional Defects in Oligothiophenes. *J. Phys. Chem. A* 2012, **116**, 2997-3003.

[69] Hindeleh, A. and Hosemann, R. Paracrystals Representing the Physical State of Matter. *J. Phys*. C 1988, **21**, 4155-4170.

[70] Rivnay, J. Noriega, R. Kline, R. J. Salleo, A. and Toney, M. F. Quantitative Analysis of Lattice Disorder and Crystallite Size in Organic Semiconductor Thin Films. *Phys. Rev. B*, 2011, **84**, 045203.

[71] Noriega, R. Rivnay, J. Vandewal, K. Koch, F. P. Stingelin, N. Smith, P. Toney, M. F. and Salleo, A. A General Relationship Between Disorder, Aggregation, and Charge Transport in Conjugated Polymers. *Nat. Mater.* 2013, **12**, 1038-1044.

[72] Kwiatkowski, J. J. Nelson, J. Li, H. Bredas, J. L. Wenzel, W. and Lennartz, C. Simulating Charge Transport in Tris(8-hydroxyquinoline) Aluminum (Alq_3). *Phys. Chem. Chem. Phys.* 2008, **10**, 1852-1858.

[73] Martinelli, N. G. Savini, M. Muccioli, L. Olivier, Y. Castet, F. Zannoni, C. Beljonne, D. and Cornil, J. Modeling Polymer Dielectric/Pentacene Interfaces: On the Role of Electrostatic Energy Disorder on Charge Carrier Mobility. *Adv. Func. Mater*. 2009, **19**, 3254-3261.

[74] Tummala, N. R. Zheng, Z. Aziz, S. G. Coropceanu, V. and Brédas, J. L. Static and Dynamic Energetic Disorders in the C_{60}, $PC_{61}BM$, C_{70}, and $PC_{71}BM$ Fullerenes. *J. Phys. Chem. Lett*. 2015, **6**, 3657-3662.

[75] Steiner, F. Foster, S. Losquin, A. Labram, J. Anthopoulos, T. D. Frost, J. M. and Nelson, J. Distinguishing the Influence of Structural and Energetic Disorder on Electron Transport in Fullerene Multi-Adducts. *Mater. Horiz.* 2015, **2**, 113-119.

[76] Martinelli, N. G.; Idé, J.; Sánchez-Carrera, R. S.; Coropceanu, V.; Brédas, J.-L.; Ducasse, L.; Castet, F.; Cornil, J.; Beljonne, D. Influence of Structural Dynamics on Polarization Energies in Anthracene Single Crystals. *J. Phys. Chem. C* 2010, **114**, 20678-20685. J. Phys. Chem. C 2010, 114, 20678–20685

[77] Sánchez-Carrera, R. S.; Paramonov, P.; Day, G. M.; Coropceanu, V.; Brédas, J. L. Interaction of Charge Carriers with Lattice Vibrations in Oligoacene Crystals from Naphthalene to Pentacene. *J. Am. Chem. Soc.* 2010, **132**, 14437–14446.

[78] Vehoff, T. Baumeier, B. Troisi, A. and Andrienko, D. Charge Transport in Organic Crystals: Role of Disorder and Topological Connectivity. *J. Am. Chem. Soc.* 2010, **132**, 11702–11708.

[79] Private communication with the Itami group, 2018.

[80] (a) Bittle, E. G.; Basham, J. I.; Jackson, T. N.; Jurchescu, O. D.; Gundlach, D. J. Mobility Overestimation Due to Gated Contacts in Organic Field-Effect Transistors. *Nat. Commun.* 2016, 7, 10908. (b) McCulloch, I.; Salleo, A.; Chabinyc, M. Avoid the Kinks
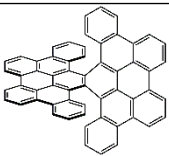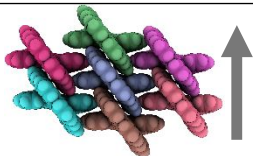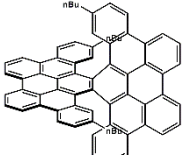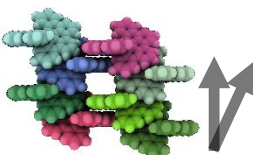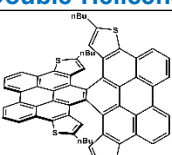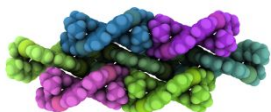
When Measuring Mobility. *Science* 2016, **352**, 1521−1522. (c) Choi, H. H.; Cho, K; Frisbie, C. D.; Sirringhaus, H.; Podzorov V., Critical assessment of charge mobility extraction in FETs. *Nat. Mater.* 2018, **17**, 2–7. (d) Rolin, C.; Kang, E.; Lee, J.-H.; Borghs, G.; Heremans, P.; Genoe, J. Charge carrier mobility in thin films of organic semiconductors by the gated van der Pauw method. *Nat. Commun.* 2017, **8**, 14975.

[81] Jackson, N. E. Kohlstedt, K. L. Savoie, B. M. de la Cruz, M. O. Schatz, G. C. Chen, L. X. and Ratner, M. A. Conformational Order in Aggregates of Conjugated Polymers. *J. Am. Chem. Soc.* 2015, **137**, 6254-6262.

[82] For select studies on side-chain engineering, see: (a) Yuan, Q.; Mannsfeld, S. C. B.; Tang, M. L.; Roberts, M.; Toney, M. F. DeLongchamp, D. M.; Bao, Z. Microstructure of Oligofluorene Asymmetric Derivatives in Organic Thin Film Transistors. *Chem. Mater.* **2008**, *20*, 2763–2772. (b) Akkerman, H. B.; Mannsfeld, S. C. B.; Kaushik, A. P.; Verploegen, E.; Burnier, L.; Zoombelt, A. P.; Saathoff, J. D.; Hong, S.; Atahan-Evrenk, S.; Liu, X.; Aspuru-Guzik, A.; Toney, M. F.; Clancy, P.; Bao, Z. Effects of Odd–Even Side Chain Length of Alkyl-Substituted Diphenylbithiophenes on First Monolayer Thin Film Packing Structure. *J. Am. Chem. Soc.* **2013**, *135*, 11006-11014. (c) Cherniawski, B. P.;

Lopez, S. A.; Burnett, E. K.; Yavuz, I.; Zhang, L.; Parkin, S. R.; Houk, K. N.; Briseno, A.

L. The Effect of Hexyl Side Chains on Molecular Conformations, Crystal Packing, and

Charge Transport of Oligothiophenes. *J. Mater. Chem. C* **2017**, *5,* 582-588. (d) Tsutsui,

Y.; Schweicher, G.; Chattopadhyay, B.; Sakurai, T.; Arlin, J.-B.; Ruzié, C.; Aliev, A.;

Ciesielski, A.; Colella, S.; Kennedy, A. R.; Lemaur, V.; Olivier, Y.; Hadji, R.; Sanguinet,

L.; Castet, F.; Osella, S.; Dudenko, D.; Beljonne, D.; Cornil, J.; Samori, P.; Seki, S.;

Geerts, Y. H. Unraveling Unprecedented Charge Carrier Mobility through Structure

Property Relationship of Four Isomers of Didodecyl[1]benzothieno[3,2-

b][1]benzothiophene. *Adv. Mater.* **2016**, *28*, 7106–7114.

TOC GRAPHIC.

	Contorted Packing	*p*-type mobility
Unsubstituted Double-Helicene	**1D transport (sensitive to traps)**	μ_{ideal} = 8.6 $\mu_{disor.}$ = 2.3 **ratio~4.0**
Substituted Double-Helicene	**2D transport (~insensitive to traps)**	μ_{ideal} = 5.7 $\mu_{disor.}$ = 5.1 **ratio~1.1**
Substituted Double-Helicene-II	**~3D transport (~unsuitable transport)**	μ_{ideal} = 5.7 $\mu_{disor.}$ = 0.4 **ratio~15**